Research Square

Preprints are preliminary reports that have not undergone peer review.
They should not be considered conclusive, used to inform clinical practice,
or referenced by the media as validated information.

Unified Nonlinear Backstepping Control of a Single-Stage Grid-Tied PV-MMC for Coordinated Arm Current Regulation, MPPT, and Voltage Balancing

Amine El Boudali

amine.elboudali-etu@etu.univh2c.ma

University of Hassan II Casablanca

Abdelmajid Abouloifa

University of Hassan II Casablanca

Ibtissam Lachkar

University of Hassan II Casablanca

Yasser Bin Salamah

King Saud University

Ouijdane Arich

University of Hassan II Casablanca

Abdelali El Aroudi

Universitat Rovira i Virgili

Research Article

Keywords:

Posted Date: November 9th, 2026

DOI: https://doi.org/10.21203/rs.3.rs-11115831/v1

License: This work is licensed under a Creative Commons Attribution 4.0 International License.
Read Full License

Additional Declarations: No competing interests reported.

Unified Nonlinear Backstepping Control of a Single-Stage Grid-Tied PV-MMC for Coordinated Arm Current Regulation, MPPT, and Voltage Balancing

Abstract

This paper presents the modeling and nonlinear control of a single-stage grid-connected photovoltaic (PV) system based on a modular multilevel converter (MMC) interfaced with the utility grid through an RL filter. The proposed control strategy is designed to simultaneously achieve efficient solar energy extraction, accurate grid current tracking, and stable MMC operation. A cascaded nonlinear control scheme based on the backstepping technique is developed, in which the inner loop regulates the MMC arm currents, while the outer loop governs the PV-side dynamics. In particular, the differential component of the arm currents is controlled to ensure accurate grid current tracking and unity power factor operation (UPF), whereas the outer loop simultaneously performs maximum power point tracking (MPPT) and capacitor voltage balancing. To facilitate the controller design and stability analysis, a nonlinear averaged model of the PV–MMC system is first derived. The main contribution is a unified nonlinear control framework that integrates arm current regulation, MPPT, and capacitor voltage balancing within a single-stage PV–MMC architecture, without an additional DC–DC conversion stage. This approach also explicitly accounts for the coupling between the PV source dynamics and the MMC submodule capacitor voltages. The proposed strategy is validated through detailed simulations using a switched model implemented in the MATLAB/Simscape Power Systems environment. The results demonstrate fast dynamic response, accurate PV voltage regulation, effective capacitor voltage balancing, and high-quality grid current injection under varying operating conditions.

Keywords: Photovoltaic systems, Modular multilevel converter, Backstepping control, Arm current control, Maximum power point tracking, Capacitor voltage balancing

1 Introduction

The rapid depletion of fossil fuel resources, combined with increasing environmental concerns and continuously growing global energy demand, has significantly accelerated the transition toward renewable energy systems. Among the available renewable

technologies, photovoltaic (PV) generation has emerged as one of the most attractive solutions due to its sustainability, scalability, and environmental compatibility [1]. Consequently, grid-connected PV systems are now becoming key elements of modern power grids, supporting clean energy integration and contributing to global decarbonization targets [2].

Power electronic converters are central to PV energy conversion systems, as they enable the adaptation of the DC output of PV sources into grid-compatible AC power [3, 4]. Over the past decades, several inverter topologies have been developed to meet the harmonics and efficiency requirements. Two-level voltage source inverters are simple and cost-effective, but they have high total harmonic distortion (THD) and increased stress and losses on the semiconductor devices [5]. To meet grid integration standards such as IEC 61850 and IEEE 1547, the THD must be below 5%. Meeting these requirements while maintaining low losses is challenging. To address these issues, several multilevel topologies have emerged, including H-bridge structures [6], neutral point clamped (NPC) converters [7, 8], and flying capacitor (FC) converters [9]. Although these topologies have demonstrated good steady-state performance in specific applications because they produce staircase voltage waveforms with low voltage stress on semiconductor devices and low THD [8–10], they suffer from inherent limitations such as complex voltage balancing requirements, high component counts, and limited scalability, particularly in medium- and high-voltage applications [11, 12].

To address these challenges, the modular multilevel converter (MMC) [13, 14], first introduced in [15], has emerged as one of the most promising topologies in modern power electronics converters for many applications [16]. Thanks to its modular structure, low harmonic distortion, reduced switching losses, and excellent scalability, the MMC has become a key enabler for high-performance energy conversion systems, including renewable energy integration, motor drives, and high-voltage transmission applications [17–20]. The MMC is made up of floating capacitor cascaded submodules (SMs), which allow flexible voltage synthesis while ensuring improved power quality and reduced device stress [21–23]. Unlike conventional multilevel converters such as cascaded H-bridge (CHB) structures [10], which require multiple isolated DC sources, the MMC is built from a large number of identical SMs—typically half-bridge or full-bridge cells—each consisting of a capacitor and controlled switching devices [24]. This modular architecture enables flexible voltage scaling through the series connection of SMs in each arm, making the MMC particularly suitable for high-voltage applications, particularly high-voltage direct current (HVDC) transmission systems, where it serves a key role according to large-scale power transfer and renewable energy integration [25–27]. Structurally, a single-phase MMC consists of an upper and a lower arm, each composed of a large number of SMs. In three-phase systems, three upper and three lower arms are used [24]. They allow to generate near-sinusoidal output waveforms with very low harmonic distortion, significantly reducing or even eliminating the need for bulky AC-side filters compared to conventional topologies. In addition, the low common-mode voltage and reduced ($\mathrm{d}v/\mathrm{d}t$) stress improve compatibility with grid-connected systems and motor drive applications. The arm inductors further enhance system robustness by limiting fault currents and improving protection capability.

Recent research has focused on addressing challenges associated with large-scale deployment. For instance, hybrid MMC configurations have been proposed to enhance fault ride-through capability and reduce energy storage requirements [27], while advanced reliability assessment methods have been developed for medium-voltage DC systems [28]. In parallel, improved modeling and simulation techniques are being explored to enable efficient real-time analysis of large HVDC networks based on MMC technology [26].

Despite this progress, the MMC still presents important challenges, mainly related to control complexity, capacitor voltage balancing, and internal circulating currents [24]. Nevertheless, the modular and repetitive nature of the MMC remains a key advantage, as it enables systematic scalability and facilitates hierarchical and distributed control design. As a result, despite its complexity, the MMC continues to be a highly attractive solution for next-generation high-power conversion systems if the control complexity is appropriately addressed.

A wide range of control strategies has been developed. These include cascaded control structures with phase-shifted PWM [29], nonlinear backstepping methods [30], model predictive control approaches [31], and sliding-mode-based techniques [32]. For instance, a unified cascaded control strategy based on sliding-mode control and filtered Proportional Integral (PI) regulation was proposed for a multilevel single-input dual-output (SIDO) boost converter, with simultaneous consideration of maximum power tracking (MPPT), power factor correction (PFC), and DC-voltage regulation [33], while backstepping strategies have also been reported for conventional grid-connected PV systems, where simultaneous MPPT, DC-link voltage regulation, and power factor correction (PFC) were successfully achieved [34]. Although this approach demonstrates the potential of nonlinear multi-objective control for multilevel PV conversion systems, it relies on a DC–DC conversion stage and does not address the internal dynamics and voltage-balancing requirements inherent to MMC-based architectures.

More recently, Active Disturbance Rejection Control (ADRC) has also been investigated for single-phase PV–MMC systems, combining an outer filtered PI controller with an inner ADRC loop to achieve grid-side power factor correction and PV voltage regulation for MPPT [35]. In parallel, recent studies have examined advanced control and modeling approaches for MMC-based renewable-energy systems, including the works reported in [36] and [37]. These contributions further highlight the importance of coordinated regulation, dynamic modeling, and power-quality control in MMC-integrated renewable-energy applications. However, the simultaneous regulation of individual MMC arm currents, PV voltage balancing, MPPT, and grid-side power quality within a unified nonlinear control framework remains insufficiently investigated.

In addition to control-oriented developments, several analytical frameworks have been proposed to better understand the internal dynamics of MMC systems, including discrete-time modeling to predict the transient response and current stress [38], imbalance analysis methods [39], adaptive PI-based strategies [40], sliding-mode regulation techniques [41], and nonlinear model-based approaches [42–44]. However, despite these significant contributions, most existing works deal with modulation, estimation, and

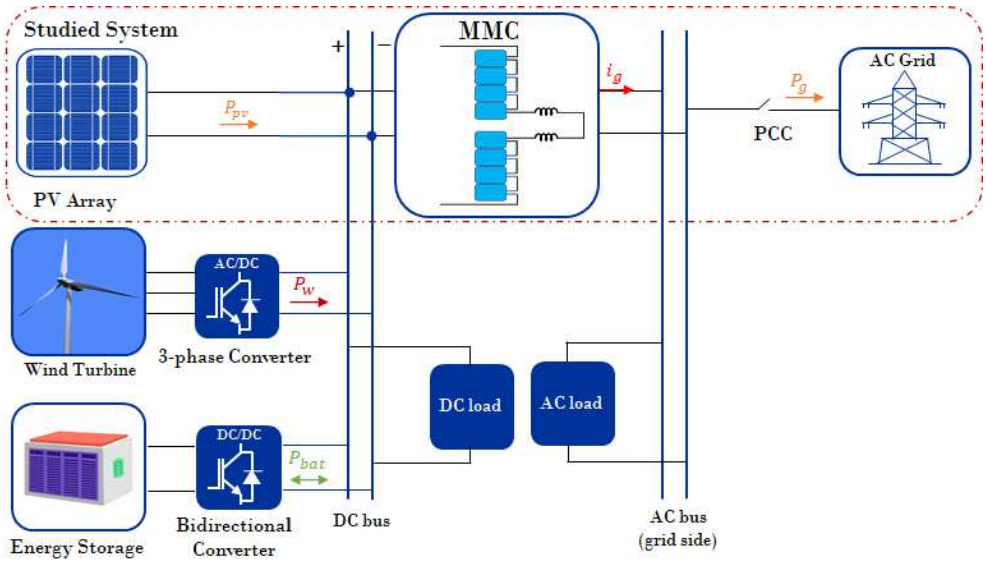


Fig. 1: Architectural diagram of an AC-DC hybrid microgrid interfaced by an MMC.

control independently and separately, and a unified nonlinear control framework for MMC-based renewable energy systems is still lacking.

Parallel to developments in inverter topologies, hybrid AC/DC microgrids have gained increasing attention as flexible architectures capable of integrating distributed energy sources feeding diverse loads. Within such systems, the MMC serves as a key interface enabling bidirectional power exchange between AC and DC networks while ensuring high power quality and modular scalability [45, 46]. However, the dynamic interaction between PV sources and MMC structures introduces additional control challenges, particularly when nonlinear system behavior, power factor correction, and maximum power extraction must be addressed simultaneously. Therefore, this paper concentrates on the PV–MMC grid interface highlighted in Fig. 1.

Motivated by these challenges, this study focuses on the nonlinear modeling and control of a grid-connected PV system based on an MMC. The primary goal is to design an effective control strategy that enables efficient power transfer from the PV source to the grid, while ensuring stable system operation and delivering high-quality injected power. Among the various nonlinear control approaches reported in the literature [47, 48], a framework based on Lyapunov theory and backstepping is developed to regulate converter dynamics and ensure stable, efficient power transfer from the PV source to the utility grid. The proposed control scheme adopts a cascaded dual-loop structure. The inner loop control makes use of a Lyapunov-based backstepping controller to regulate the MMC currents to perform power factor correction (PFC) at the grid side. The outer control loop, also designed using backstepping, aims to fulfill two main objectives: i) maximum power point tracking (MPPT) from the PV source and ii) voltage balancing between the PV capacitor voltages to guarantee the MMC-based PV system operates correctly.

The main contributions of this work are summarized below:

- A nonlinear averaged dynamic model of a grid-connected PV–MMC system is developed, suitable for control design and analysis.
- A Lyapunov-based backstepping inner current control loop is proposed to ensure stable current regulation and unity power factor (UPF) operation at the grid interface.
- An outer voltage control loop based on the backstepping approach is formulated to achieve simultaneous MPPT and PV voltage balancing.
- The proposed control scheme is integrated into a unified nonlinear control framework, enabling coordinated energy management between the PV source and the electrical grid.

The effectiveness of the proposed control architecture is validated through detailed simulations, demonstrating improved dynamic performance, accurate PV voltage regulation, enhanced power quality at the grid interface, and precise tracking of the arm current references. Unlike existing approaches, the proposed strategy integrates a dual-loop backstepping control framework that simultaneously ensures MPPT operation, PV voltage balancing, PFC, and accurate arm current tracking within a unified control structure. To the best of the authors' knowledge, most existing works address these control objectives separately or partially [30, 49, 50]. In contrast, a fully integrated control scheme for PV-MMC systems has been implemented for the first time in this work to achieve the objectives of accurate arm current tracking, PFC, MPPT operation, and PV voltage balancing.

The rest of this paper is structured as follows. Section 2 presents the system description and mathematical modeling. Section 3 introduces the control objectives and provides the steady-state analysis. Section 4 details the design of the nonlinear controller. Section 5 discusses the simulation results. Finally, Section 6 concludes the paper.

2 System Architecture and Mathematical Modeling of the PV–MMC System

2.1 Description of the Studied System

Fig. 2 depicts the circuit diagram of the system under study in this paper. It consists of a PV–fed grid-connected MMC composed of eight SMs, four SMs at the top side and other four SMs at the bottom side. Each SM consists of a capacitor C and a pair of semiconductor switches. Moreover, each arm of the converter contains an inductor with inductance L and an equivalent series resistor r. The MMC is interfaced with the AC grid through a coupling filter characterized by the inductor with inductance L_g and an equivalent series resistor r_g.

Each SM within the MMC operates in four distinct circuit configurations (see Fig. 3), determined by the switching signals $\mu_{x,u} \in \{+1, -1\}$, where $x = 1, \ldots, 4$, and $\mu_{y,l} \in \{+1, -1\}$, where $y = 5, \ldots, 8$. When $\mu_{x,u} = +1$ or $\mu_{y,l} = +1$, the corresponding SM is

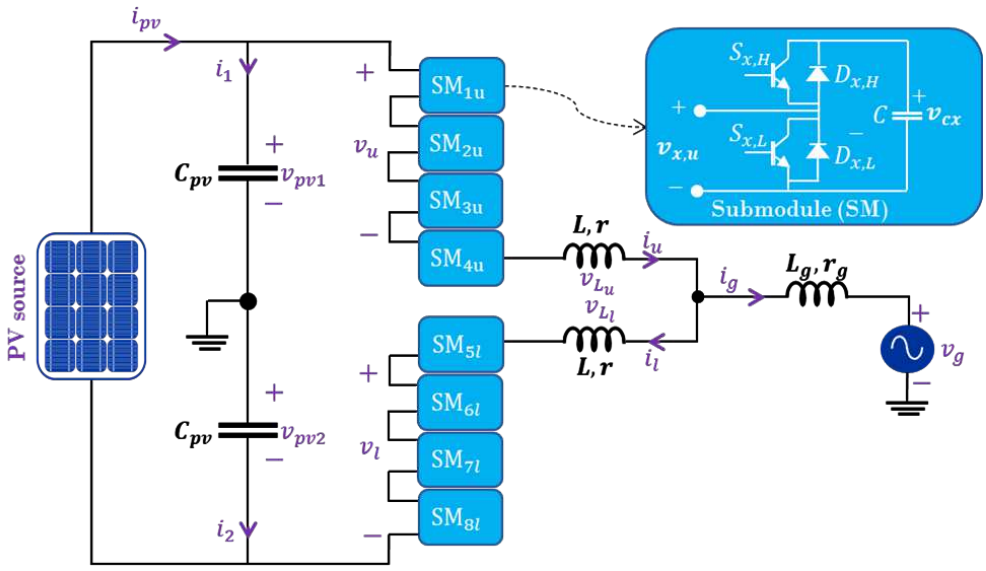


Fig. 2: Simplified schematic electrical diagram of a PV-fed grid-tied MMC.

inserted, and its output voltage equals the capacitor voltage $v_{c,x}$ or $v_{c,y}$. Conversely, when $\mu_{x,u} = -1$ or $\mu_{y,l} = -1$, the SM is bypassed, resulting in a zero output voltage.

The sign of the SM current plays a key role in determining the SMs internal behavior. A positive current (i.e., $i_u > 0$ for the upper arm or $i_l > 0$ for the lower arm) corresponds to current flowing from the upper to the lower terminal of the SM, leading to capacitor charging when the SM is inserted. In contrast, a negative current ($i_u < 0$ or $i_l < 0$) indicates current flowing in the opposite direction, resulting in the capacitor discharging. Moreover, the current direction determines the conduction paths through the semiconductor devices (IGBTs and antiparallel diodes), leading to the four operating configurations illustrated in Fig. 3. In the figure, only the SM in the upper arm is shown. For that arm, two IGBTs $S_{x,H}$ and $S_{x,L}$ are used with their antiparallel diodes $D_{x,H}$ and $D_{x,L}$. Similarly, two IGBTs $S_{y,H}$ and $S_{y,L}$ are used in the lower arm with their antiparallel diodes $D_{y,H}$ and $D_{y,L}$. The differential equation describing the behavior of the capacitor voltage $v_{x,u}$ of an upper SM ($\mathrm{SM}_{x,u}$, $x = 1 \dots 4$) and a lower SM ($\mathrm{SM}_{y,l}$, $y = 5 \dots 8$) can be written as:

$$C\frac{dv_{x,u}}{dt} = \frac{1+\mu_{x,u}}{2}\, i_u \tag{1a}$$

$$C\frac{dv_{y,l}}{dt} = \frac{1+\mu_{y,l}}{2}\, i_l \tag{1b}$$

2.2 Mathematical Modeling

Using KVL and KCL, the dynamic model governing the circuit behavior can be obtained. The following compact form can be used to express this model:

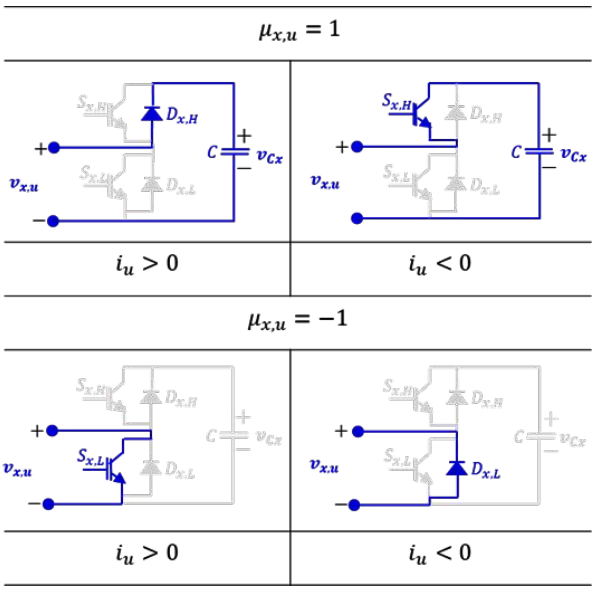


Fig. 3: Upper SM circuit configurations according to the values of the driving signals and the sign of the current i_u.

$$L\frac{d\boldsymbol{i_{ul}}}{dt} = \boldsymbol{Z}_{ul}\,\boldsymbol{i}_{ul} + v_g\,\boldsymbol{M}_1 + \boldsymbol{M}_2\,(\boldsymbol{v}_{pv} - \boldsymbol{v}_{ul}) \tag{2a}$$

$$C_{pv}\frac{d\boldsymbol{v}_{pv}}{dt} = i_{pv}\,\boldsymbol{M}_3 - \boldsymbol{i}_{ul} \tag{2b}$$

where the variables $\boldsymbol{i}_{ul}$, $\boldsymbol{v}_{pv}$, $\boldsymbol{v}_{ul}$, the matrices $\boldsymbol{Z}_{ul}$, $\boldsymbol{M}_1$, $\boldsymbol{M}_2$, $\boldsymbol{M}_3$ and the coefficient δ appearing in the previous equations are given by:

$$\boldsymbol{i}_{ul} = \begin{pmatrix} i_u \\ i_l \end{pmatrix}, \quad \boldsymbol{v}_{pv} = \begin{pmatrix} v_{pv1} \\ v_{pv2} \end{pmatrix}, \quad \boldsymbol{v}_{ul} = \begin{pmatrix} v_u \\ v_l \end{pmatrix}$$

$$\boldsymbol{Z}_{ul} = \frac{1}{2+\delta}\begin{pmatrix} -(1+\delta)r - \delta r_g & \delta r_g - r \\ \delta r_g - r & -(1+\delta)r - \delta r_g \end{pmatrix},$$

$$\boldsymbol{M}_1 = \frac{\delta}{2+\delta}\begin{pmatrix} -1 \\ 1 \end{pmatrix}, \; \boldsymbol{M}_2 = \frac{1}{2+\delta}\begin{pmatrix} 1+\delta & 1 \\ 1 & 1+\delta \end{pmatrix},$$

$$\boldsymbol{M}_3 = \begin{pmatrix} 1 \\ 1 \end{pmatrix}, \quad \delta = \frac{L}{L_g}$$

The upper-arm voltage v_u and lower-arm voltage v_l are, respectively, determined by the SM binary signals $\mu_{u,x}$ and $\mu_{y,l}$ and the corresponding capacitor voltages v_{cx} and v_{cy} according to the following expression:

$$v_u = \sum_{x=1}^{4} \frac{1+\mu_{x,u}}{2} v_{cx} \tag{3a}$$

$$v_l = \sum_{y=5}^{8} \frac{1+\mu_{y,l}}{2} v_{cy} \tag{3b}$$

These voltages are essential for capturing the MMC dynamics and enabling the design of the associated control strategy.

The PWM scheme uses eight carrier signals that are equally phase-shifted by $\pi/4$. The upper SMs use the carriers with phase shifts of 0, $\pi/2$, π, and $3\pi/2$, while the lower SMs are assigned the carriers with phase shifts of $\pi/4$, $3\pi/4$, $5\pi/4$, and $7\pi/4$. This allows a uniform distribution of switching events and helps reduce voltage ripple at the converter voltages and currents. [51].

Using (2a) and (2b) as a basis, the system is first represented by a switched model. The associated averaged model is then derived, leading to the following expression:

$$L\frac{d\bar{\boldsymbol{i}}_{ul}}{dt} = \boldsymbol{Z}_{ul}\,\bar{\boldsymbol{i}}_{ul} + v_g\,\boldsymbol{M}_1 + \boldsymbol{M}_2\,(\overline{\boldsymbol{v}}_{pv} - \overline{\boldsymbol{v}}_{ul}) \tag{4a}$$

$$C_{pv}\frac{d\overline{\boldsymbol{v}}_{pv}}{dt} = \bar{i}_{pv}\,\boldsymbol{M}_3 - \bar{\boldsymbol{i}}_{ul} \tag{4b}$$

where overbar stands for averaging within one switching period.

3 Control Objectives and Steady-State Analysis

The control objectives for the grid-tied PV-MMC system are summarized below:

i) Accurate tracking of arm current references: The controller's primary objective is to provide precise tracking of the reference current vector of the MMC's both upper and lower arms $\boldsymbol{i}_{ul}^{d} = \left(i_u^d \;\; i_l^d\right)^{\intercal}$. By regulating the arm currents, the converter can control the power exchanged with the grid while maintaining the desired dynamic performance.

ii) Power factor correction: this involves feeding power from the solar panels into the grid with a UPF. The current supplied to the grid, i_g, needs to be a sinusoidal waveform that complies with its reference, $i_g^d = \beta v_g$, and is synchronized with the grid voltage.

iii) Real-time tracking of the maximum power point (MPP) through an MPPT algorithm: optimizing solar energy extraction by keeping the system close to the MPP. This is achieved by regulating the PV voltage vector $\boldsymbol{v}_{pv}$ to its setpoint $\boldsymbol{v}_{pv}^{d}$ dictated by the MPPT algorithm.

iv) Balancing of voltages v_{pv1} and v_{pv2}: ensuring that the average of the voltages v_{pv1} and v_{pv2} are identical to their reference $v_{pv}^{d}/2$ in steady-state operation with the desired dynamic performances.

Under steady-state and stable operating conditions, the grid voltage and current exhibit sinusoidal waveforms and remain in phase. They can thus be expressed as follows:

$$v_g(t) = V_g\sqrt{2}\sin(\omega t) \tag{5}$$

$$i_g(t) = I_g\sqrt{2}\sin(\omega t) \tag{6}$$

The upper and lower arm currents are expressed in terms of the PV current and the grid current as follows:

$$\boldsymbol{i}_{ul} = i_{pv}\,\boldsymbol{M}_3 + \frac{i_g}{2}\,\boldsymbol{M}_4, \quad \boldsymbol{M}_4 = \begin{pmatrix}1 & -1\end{pmatrix}^\intercal \tag{7}$$

Substituting (5), (6), and (7) into (2a), we obtain the following relationship, which yields the steady-state expressions for the arm voltages:

$$\boldsymbol{v}_{ul} = \boldsymbol{V}_{ul,dc}\,\boldsymbol{M}_3 - V_{ac}\sin(\omega t + \varphi)\,\boldsymbol{M}_4 \tag{8}$$

where $\boldsymbol{V}_{ul,dc}$, V_{ac} and φ are given by the following expressions:

$$\begin{aligned}
\boldsymbol{V}_{ul,dc} &= \boldsymbol{v}_{pv} - r i_{pv}\,\boldsymbol{M}_4 \\
V_{ac} &= \frac{1}{\delta - 1}\sqrt{\begin{matrix}[(2\delta r_g + (\delta-1)r)\,I_g + 2(\delta-1)V_g]^2 \\ + [(\delta+1)L\omega I_g]^2\end{matrix}}, \\
\varphi &= \tan^{-1}\left(\frac{(\delta+1)L\omega I_g}{(2\delta r_g + (\delta-1)r)I_g + 2(\delta-1)V_g}\right)
\end{aligned}$$

Considering the upper- and lower-arm voltage expressions and using (8), the steady-state control inputs $\boldsymbol{u}_{ul} = \begin{pmatrix}u_u & u_l\end{pmatrix}^\intercal$ of these arms are given by:

$$\boldsymbol{u}_{ul} = -\left(\boldsymbol{M}_3 - \boldsymbol{V}_1\right) + \boldsymbol{V}_2\,\sin(\omega t + \varphi) \tag{9}$$

The vectors $\boldsymbol{V}_1$ and $\boldsymbol{V}_2$ are expressed as:

$$\boldsymbol{V}_1 = \begin{pmatrix}\frac{V_{u,dc}}{v_{cu}} \\ \frac{V_{l,dc}}{v_{cl}}\end{pmatrix}, \qquad \boldsymbol{V}_2 = \begin{pmatrix}\frac{V_{ac}}{v_{cu}} \\ \frac{V_{ac}}{v_{cl}}\end{pmatrix}$$

where $v_{cu} = \sum_{x=1}^{4} v_{cx}$ and $v_{cl} = \sum_{y=5}^{8} v_{cy}$

By neglecting the voltage drops in r_g, r, and L and considering that the control inputs in u_{ul} are bounded within the interval $(-1, 1)$, the following condition can be derived for the system to operate correctly:

$$v_{pv1} + v_{pv2} > 4V_g \tag{10}$$

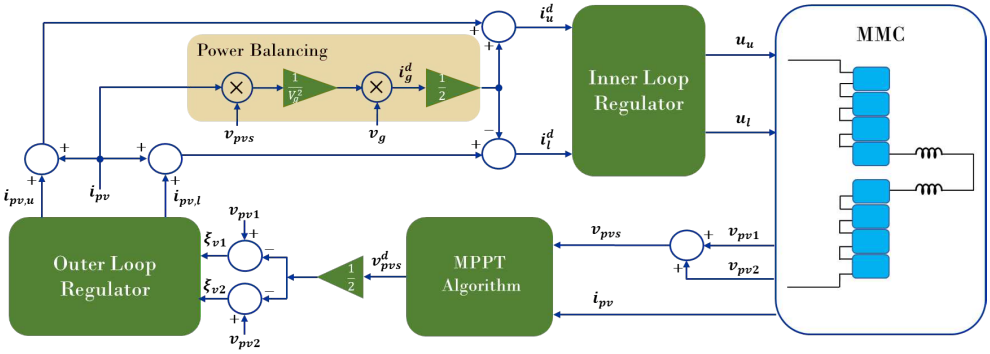


Fig. 4: Structure of the proposed controller.

This condition reflects a fundamental operating requirement of the converter: the DC bus voltage must be sufficiently high to ensure proper modulation and controllability of the arm voltages. More precisely, it guarantees that the converter can produce the necessary AC voltage in accordance with the grid voltage without saturation. Therefore, under ideal conditions, the DC bus voltage must exceed four times the peak value of the grid voltage to maintain stable operation and ensure effective power transfer.

4 Control Architecture

Building upon the control objectives defined in the previous section, as well as the inherent properties of the MMC topology, a cascaded two-loop control structure is employed, as depicted in Fig. 4. The proposed strategy is composed of an outer voltage regulation loop and an inner current control loop. The outer loop is responsible for regulating the PV-side voltages while ensuring the MPPT, whereas the inner loop guarantees accurate tracking of the arm currents. To enhance system stability and dynamic performance, nonlinear backstepping controllers are developed for both control loops.

4.1 Inner Loop Design

To meet grid requirements, the inner control loop is designed to ensure UPF. This is achieved by setting the grid current to be sinusoidal and in phase with the grid voltage. In this work, the control strategy is based on the direct regulation of the arm current vector $\boldsymbol{i}_{ul}$. This choice relies on the relationship between the arm currents and the grid current, given by $(i_g = i_u - i_l)$. Therefore, accurate tracking of the arm currents ensures the desired grid current behavior and enables PFC. To this end, a backstepping controller is designed to regulate $\boldsymbol{i}_{ul}$, providing robust tracking performance under varying operating conditions.

To guarantee accurate tracking of the arm current references, the following tracking error vector is defined:

$$\boldsymbol{\xi}_i = L\left(\bar{\boldsymbol{i}}_{ul} - \bar{\boldsymbol{i}}_{ul}^{d}\right) \tag{11}$$

Its time derivative is:

$$\dot{\boldsymbol{\xi}}_i = \boldsymbol{Z}_{ul}\,\bar{\boldsymbol{i}}_{ul} + v_g\,\boldsymbol{M}_1 + \boldsymbol{M}_2\,(\overline{\boldsymbol{v}}_{pv} - \overline{\boldsymbol{v}}_{ul}) - L\frac{d\bar{\boldsymbol{i}}_{ul}^{d}}{dt} \tag{12}$$

A quadratic Lyapunov function candidate is selected as follows:

$$\boldsymbol{V}_i = \frac{1}{2}\boldsymbol{\xi}_i^{\intercal}\boldsymbol{\xi} \tag{13}$$

Its time derivative is given by the following expression:

$$\dot{\boldsymbol{V}}_i = \boldsymbol{\xi}_i^{\intercal}\left(\boldsymbol{Z}_{ul}\,\bar{\boldsymbol{i}}_{ul} + v_g\,\boldsymbol{M}_1 + \boldsymbol{M}_2\,(\overline{\boldsymbol{v}}_{pv} - \overline{\boldsymbol{v}}_{ul}) - L\frac{d\bar{\boldsymbol{i}}_{ul}^{d}}{dt}\right) \tag{14}$$

Let $\boldsymbol{Q}_i = -\mathrm{diag}(k_{i1}, k_{i2})$ be a negative definite matrix, where k_{i1} and k_{i2} are positive constants. If the error dynamics are enforced to be as follows:

$$\dot{\boldsymbol{\xi}}_i = \boldsymbol{Q}_i\,\boldsymbol{\xi}_i \tag{15}$$

Then, $\boldsymbol{Q}_i$ is a negative definite matrix; it follows that $\dot{\boldsymbol{V}}_i$ is negative. Consequently, the tracking error vector $\boldsymbol{\xi}_i$ converges asymptotically to zero, ensuring stable tracking of the arm current references.

By substituting the system state equations into the derivative of the Lyapunov function (14), the stabilizing voltage can be expressed as follows:

$$\overline{\boldsymbol{v}}_{ul} = \overline{\boldsymbol{v}}_{pv} + \boldsymbol{M}_2^{-1}\left(\boldsymbol{Z}_{ul}\,\bar{\boldsymbol{i}}_{ul} + v_g\,\boldsymbol{M}_1 - L\frac{d\bar{\boldsymbol{i}}_{ul}^{d}}{dt} - \boldsymbol{Q}_i\,\boldsymbol{\xi}_i\right) \tag{16}$$

Combining (16), (3a) and (3b), the following backstepping control law is derived:

$$\begin{aligned}\boldsymbol{u}_{ul} = \boldsymbol{V}_3^{-1}\Bigg(&\overline{\boldsymbol{v}}_{pv} + \boldsymbol{M}_2^{-1}\Big(\boldsymbol{Z}_{ul}\bar{\boldsymbol{i}}_{ul} + v_g\boldsymbol{M}_1 \\ &- L\frac{d\bar{\boldsymbol{i}}_{ul}^{d}}{dt} - \boldsymbol{Q}_i\boldsymbol{\xi}_i\Big) - \boldsymbol{V}_4\Bigg)\end{aligned} \tag{17}$$

where the vectors $\boldsymbol{V}_3$ and $\boldsymbol{V}_4$ are given by:

$$\boldsymbol{V}_3 = \frac{1}{2}\begin{pmatrix} v_{cu} & 0 \\ 0 & v_{cl}\end{pmatrix}, \qquad \boldsymbol{V}_4 = \frac{1}{2}\begin{pmatrix} v_{cu} \\ v_{cl}\end{pmatrix}$$

Remark 1 Consider the PV–MMC system depicted in Fig. 2, which is described by the averaged state-space model given in (4a). In closed-loop operation, the system dynamics can be expressed in the error coordinates as follows:

$$\dot{\boldsymbol{\xi}}_i = \boldsymbol{Q}_i\,\boldsymbol{\xi}_i \tag{18}$$

Remark 2 The reference vector of the upper and lower arm currents is given by:

$$\boldsymbol{i}_{ul}^{d} = \boldsymbol{i}_{pv,c} + \boldsymbol{M}_4 \frac{i_g^d}{2} \tag{19}$$

where $\boldsymbol{i}_{ul}^{d}$ and $\boldsymbol{i}_{pv,c}$ denote the reference arm current vector and the control input vector generated by the outer loop, respectively. The control input $\boldsymbol{i}_{pv,c}$ will be explicitly designed in Section 4.2. To perform PFC on the grid side, the grid current reference is selected as follows:

$$i_g^d(t) = \beta\, v_g(t) \tag{20a}$$

The signal β is a state variable provided by the outer voltage loop. Ideally, in steady-state operation, this signal is given by:

$$\beta_{\text{ss}} := B = \frac{V_{pv} I_{pv}}{V_g^2} \tag{20b}$$

4.2 MPPT and Outer Voltage Control

To ensure proper energy extraction and balanced operation of the PV sources, the proposed control strategy regulates the PV voltage vector $\boldsymbol{v}_{pv}$ toward the reference value $v_{pv}^d/2$. This choice guarantees that the total PV voltage follows the optimal value $\boldsymbol{v}_{pv}^d$ provided by the MPPT algorithm. Accordingly, two main control objectives are considered:

1. ensuring the tracking of the maximum power point, and
2. maintaining the voltage balance between v_{pv1} and v_{pv2}.

To achieve these objectives, a backstepping-based control law is designed in the outer control loop to ensure accurate tracking and closed-loop stability.

Based on the tracking error defined in (11), the arm current vector $\boldsymbol{i}_{ul}$ can be expressed as follows:

$$\bar{\boldsymbol{i}}_{ul} = \bar{\boldsymbol{i}}_{ul}^{d} + \frac{1}{L}\boldsymbol{\xi}_i \tag{21}$$

A sum-and-difference transformation is applied to the PV voltages such that $\boldsymbol{v}_{pv,m} = \begin{pmatrix} v_{pv,s} & v_{pv,d} \end{pmatrix}^{\intercal}$, where $v_{pv,s} = v_{pv1} + v_{pv2}$ and $v_{pv,d} = v_{pv1} - v_{pv2}$. By applying this coordinate transformation, one can write:

$$C_{pv} \frac{d\overline{\boldsymbol{v}}_{pv,m}}{dt} = \boldsymbol{N}_1\, \boldsymbol{i}_{pv,c} + \boldsymbol{N}_2\, \bar{i}_g^d + \boldsymbol{N}_1\, \boldsymbol{\xi}_i \tag{22}$$

where the vector $\boldsymbol{i}_{pvc}$ and the constant matrices $\boldsymbol{N}_1$ and $\boldsymbol{N}_2$ can be expressed as follows:

$$\boldsymbol{i}_{pv,c} = \begin{pmatrix} i_{pvc,u} \\ i_{pvc,l} \end{pmatrix}, \quad \boldsymbol{N}_1 = \begin{pmatrix} 1 & 1 \\ 1 & -1 \end{pmatrix}, \quad \boldsymbol{N}_2 = \begin{pmatrix} 0 \\ -1 \end{pmatrix}$$

To ensure accurate tracking of the PV voltage references, the following weighted tracking error vector is defined:

$$\boldsymbol{\xi}_v = C_{pv} \left(\overline{\boldsymbol{v}}_{pv,m} - \overline{\boldsymbol{v}}_{pv,m}^{d} \right) \tag{23}$$

Taking the time derivative yields:

$$\dot{\boldsymbol{\xi}}_v = \boldsymbol{N}_1\, \boldsymbol{i}_{pv,c} + \boldsymbol{N}_2\, \bar{i}_g^d + \boldsymbol{N_1}\, \xi_i - C_{pv} \frac{d\overline{\boldsymbol{v}}_{\boldsymbol{pv,m}}^{\boldsymbol{d}}}{dt} = \boldsymbol{Q_v}\, \boldsymbol{\xi}_v \tag{24}$$

where $\boldsymbol{Q}_v = -\mathrm{diag}(k_{v1}, k_{v2})$ is a negative-definite diagonal gain matrix. The coefficients k_{v1} and k_{v2} are positive tuning parameters. To guarantee asymptotic stability, the following quadratic Lyapunov candidate function is selected:

$$\boldsymbol{V}_v = \frac{1}{2} \boldsymbol{\xi}_v^{\intercal} \boldsymbol{\xi}_v \tag{25}$$

Its time derivative is given by:

$$\dot{\boldsymbol{V}}_v = \boldsymbol{\xi}_v^{\intercal} \left(\boldsymbol{N}_1\, \boldsymbol{i}_{pv,c} + \boldsymbol{N}_2\, \bar{i}_g^d + \boldsymbol{N}_1\, \boldsymbol{\xi}_v - C_{pv} \frac{d\overline{\boldsymbol{v}}_{pv,m}^{d}}{dt} \right) \tag{26}$$

By substituting (24), the following control input is obtained :

$$\boldsymbol{i}_{pv,c} = \boldsymbol{N}_1^{-1} \left(C_{pv} \frac{d\overline{\boldsymbol{v}}_{pv,m}^{d}}{dt} - \boldsymbol{N}_2\, \bar{i}_g^d - \boldsymbol{N}_1\, \xi_i - \boldsymbol{Q}_v\, \boldsymbol{\xi}_v \right) \tag{28}$$

Remark 3 Let us consider the PV–MMC system shown in Fig. 2, described by the averaged state-space representation in (4b) along with the control law introduced in (28). When operating in closed loop, the system dynamics can be conveniently expressed in the error-coordinate framework as follows:

$$\dot{\boldsymbol{\xi}}_v = \boldsymbol{Q}_v\, \boldsymbol{\xi}_v \tag{30}$$

5 Results and Discussion

The overall PV–MMC system and its corresponding control strategy are depicted in Fig. 5. The model is developed in MATLAB/SIMULINK using the SimPowerSystems toolbox with a fixed-step ODE1 (Euler) solver. All detailed specifications under atmospheric conditions are outlined in Tables **??** and 2, the system parameters and controller specifications are summarized in Table 3.

The closed-loop performance is evaluated under two operating scenarios: (i) varying solar irradiance with constant temperature, and (ii) varying temperature with constant irradiance. These scenarios assess the robustness of the proposed control strategy under environmental variations.

5.1 Dynamic Performance under Step Variations of Solar Irradiance

Fig. 6 illustrates the irradiance profile applied to evaluate the dynamic performance of the proposed grid-connected PV–MMC control strategy, while the temperature is

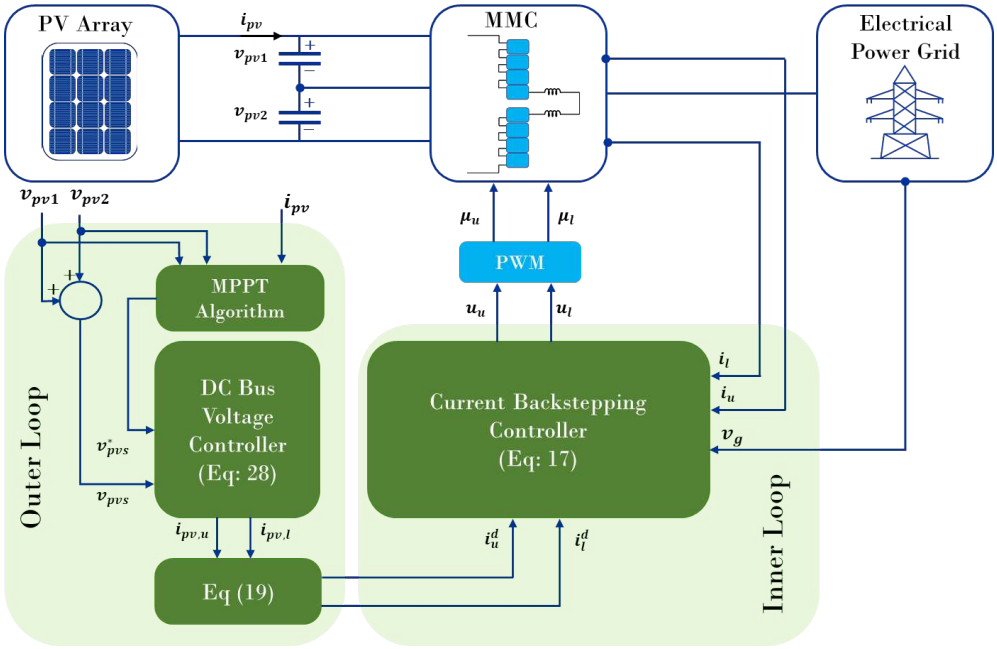


Fig. 5: Structure of the planned controller.

Table 1: Electrical characteristics of the PV panel

Parameter	**Symbol**	**Value**
PV Array (1Soltech 1STH-220-P, 32S×4P)		
Maximum power voltage	V_{mp}	29.3 V
Maximum power current	I_{mp}	7.47 A
Maximum power	P_m	218.87 W
Short circuit current	I_{SC}	7.97 A
Open circuit voltage	V_{OC}	36.6 V

Table 2: Maximum power point (MPP) characteristics under different operating conditions.

MPP	G **(W/m²)**	T **(°C)**	V_{MPP} **(V)**	P_{MPP} **(W)**
MPP1	1000	25	973.6	28020
MPP2	1200	25	930.2	33270
MPP3	800	25	943.5	22580
MPP4	1000	45	851.9	25700
MPP5	1000	15	980.6	29120

Table 3: PV–MMC system parameters.

Category	Symbol	Value
Controlled system characteristics.		
Grid parameters	v_g	$220\sqrt{2}\,\mathrm{V},\ 50\,\mathrm{Hz}$
	$r_g,\ L_g$	$1\,\mathrm{m\Omega},\ 1\,\mathrm{mH}$
PV-side parameters	C_{pv}	$1\,\mathrm{mF}$
MMC parameters	C_{SM}	$2\,\mathrm{mF}$
	$r,\ L$	$1\,\mathrm{m\Omega},\ 1\,\mathrm{mH}$
	f_e	$10\,\mathrm{kHz}$
Main control design parameters.		
Inner current regulator	$k_{i1},\ k_{i2}$	$5 \times 10^4\,\mathrm{s}^{-1}$
Outer voltage regulator	$k_{v1},\ k_{v2}$	$50\,\mathrm{s}^{-1}$

maintained constant at 25°C. The corresponding system responses are presented in Figs. 7–10. The DC bus voltage v_{pv} shown in Fig. 7a remains well regulated despite these variations, demonstrating the effectiveness of the outer control loop. The PV voltages v_{pv1} and v_{pv2} in Fig. 7b accurately track their reference values with minimal steady-state error, ensuring proper MPPT operation. The system exhibits a fast dynamic response with negligible overshoot and short settling times in response to irradiance variations, confirming the good damping characteristics of the proposed control strategy. As illustrated in Fig. 7c, both the PV power and the grid power rapidly adapt to changes in irradiance, indicating effective power extraction from the PV source and proper power injection into the grid. (see Table 2). The upper and lower arm voltages in Fig. 8a and Fig. 8b remain well balanced, while the arm currents in Fig. 8c closely follow their reference signals with smooth sinusoidal waveforms, highlighting the effectiveness of the inner current control loop. The grid current shown in Fig. 9a remains sinusoidal and well synchronized with the grid voltage. This is further confirmed by the phase alignment in Fig. 9b, demonstrating unity power factor operation. The harmonic spectrum in Fig. 9c reveals a very low distortion level. For a quantitative assessment of power quality, the THD of the grid current under different irradiance levels is reported in Table 4. As observed, the THD remains below 0.3% across all operating conditions, reaching its minimum at nominal irradiance (1000 W/m^2). Finally, the external signal β in Fig. 10a adapts appropriately to irradiance variations. In contrast, the internal control signals u in Fig. 10b remain bounded and smooth, ensuring the practical feasibility of the proposed control strategy.

In general, the obtained results confirm the effectiveness of the proposed control strategy in ensuring fast dynamic response, accurate reference tracking, balanced operation, and robust performance under varying irradiance conditions.

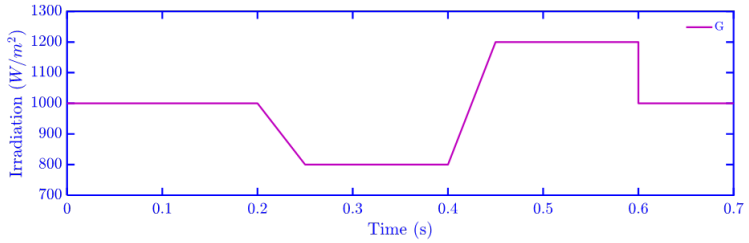
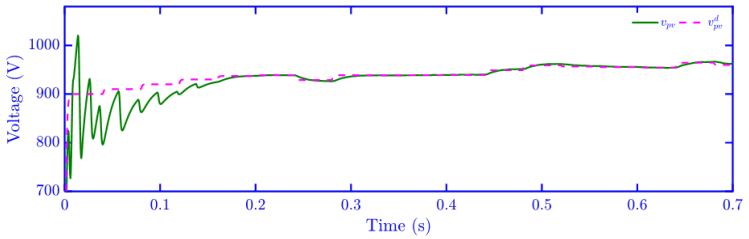
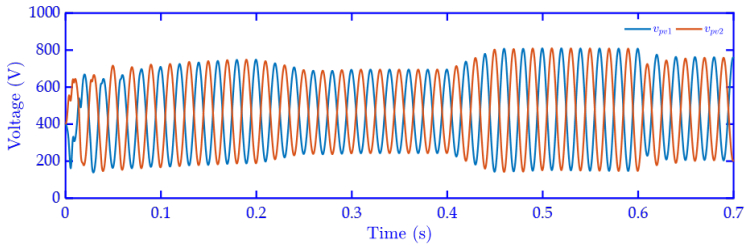


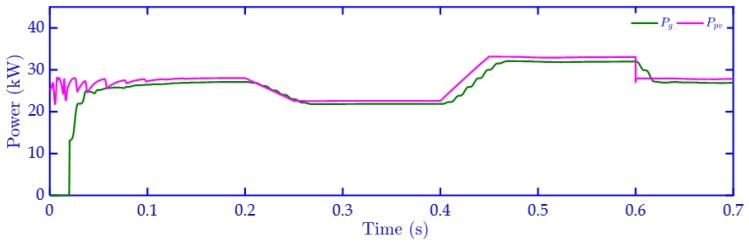
Fig. 6: Irradiance change profile.



(a) DC bus voltage and its intended reference.

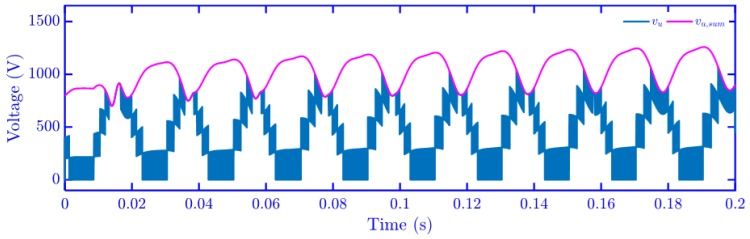


(b) Actual PV voltages (v_{pv1}) and (v_{pv2}).

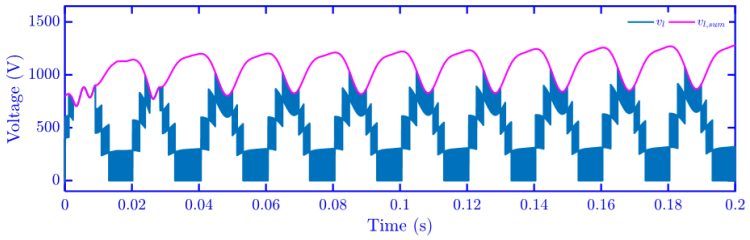


(c) Active power injected into the grid from PV panels.

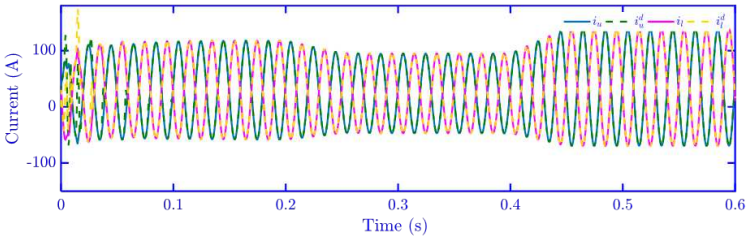
Fig. 7: Dynamic performance of the proposed control strategy under varying irradiation: (a) DC bus voltage, (b) PV voltages, and (c) Grid-injected power.



(a) Voltage of the upper arm.



(b) Voltage of the lower arm.

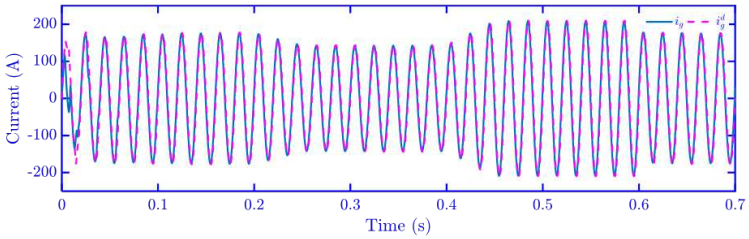


(c) Arm currents.

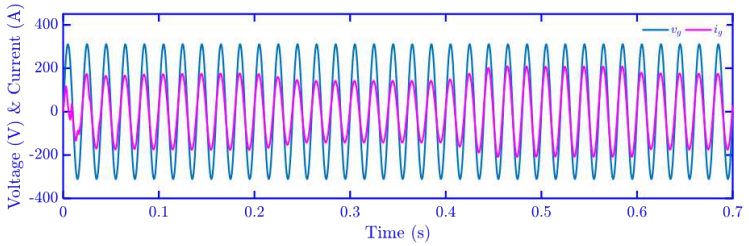
Fig. 8: Dynamic performance of the proposed control strategy under varying irradiation of voltages and currents of the arm.

5.2 Dynamic Performance under Step Variations of Temperature

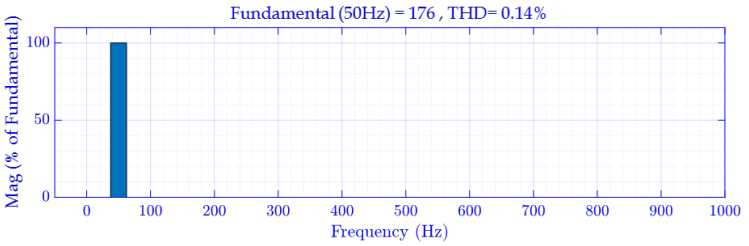
Fig. 11 presents the temperature variation profile applied to evaluate the dynamic performance of the proposed PV–MMC control strategy, while the irradiance is maintained constant at 1000 W/m^2. The corresponding system responses are illustrated in Figs. 12–14. The DC bus voltage v_{pv} in Fig. 12a remains well regulated despite temperature changes, confirming the effectiveness of the outer voltage control loop. The PV voltages v_{pv1} and v_{pv2} in Fig. 12b accurately track their reference values with minimal steady-state error, ensuring proper MPPT operation. The system exhibits a fast dynamic response with negligible overshoot during temperature transitions. As illustrated in Fig. 12c, both the PV panel power and the grid power vary smoothly with temperature (see Table 2), reflecting the natural dependence of PV characteristics on temperature variations.



(a) Actual grid current and its reference.



(b) Grid voltage and current showing PFC performance.

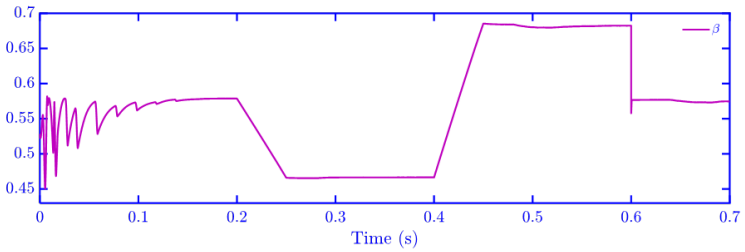


(c) Grid current spectrum showing THD.

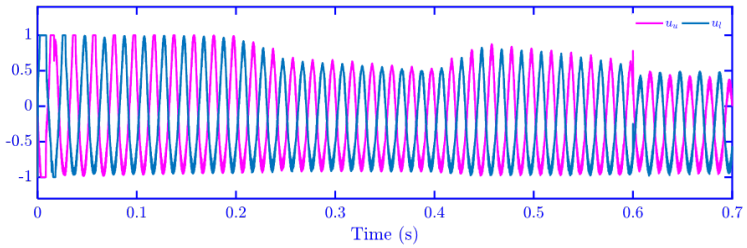
Fig. 9: Dynamic performance of the proposed control strategy under varying irradiation: (a) Grid current, (b) PFC performance, (c) FFT spectrum.

Table 4: THD of the grid current under different irradiance levels.

Irradiance (W/m^2)	THD (%)
800	0.23
1000	0.14
1200	0.16



(a) External signal β.



(b) Internal signals u_u and u_l.

Fig. 10: Dynamic performance of the proposed control strategy under varying irradiation: (a) external control signal β, and (b) Internal signals.

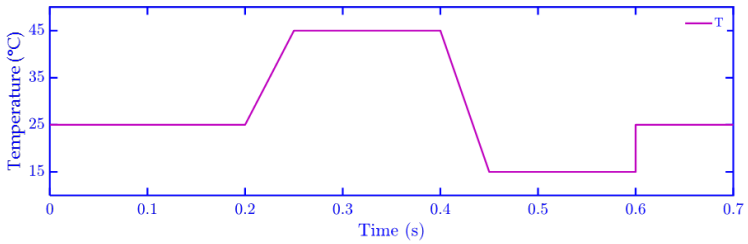
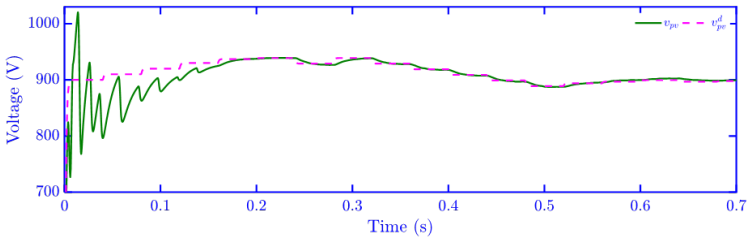


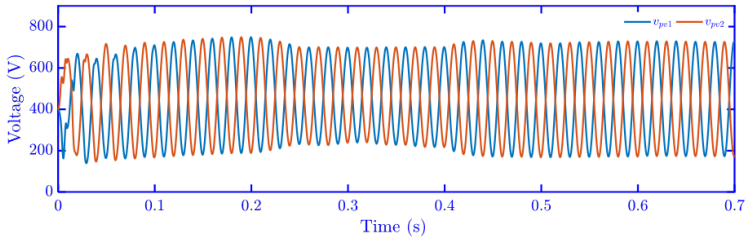
Fig. 11: Temperature pattern.

The arm currents in Fig. 13a maintain sinusoidal waveforms and closely follow their reference signals, while the grid current in Fig. 13b remains well synchronized with the grid voltage, confirming unity power factor operation. This is further supported by the phase alignment shown in Fig. 13c. The external signal β in Fig. 14a adapts appropriately to temperature variations, indicating an appropriate adaptation of the operating point to temperature variations, whereas the internal control signals u in Fig. 14b remain bounded and smooth. The harmonic performance is summarized in Table 5, where the THD remains very low under all temperature conditions (0.14% at 25° C, 0.22% at 15° C, and 0.27% at 45° C), demonstrating the robustness of the proposed control strategy and ensuring high power quality.

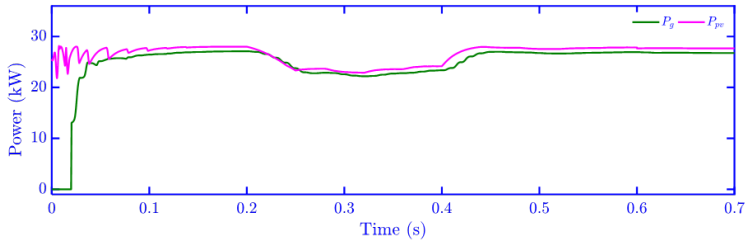
The obtained results demonstrate the stability, accurate tracking performance, and robustness of the proposed control strategy under temperature variations.



(a) DC bus voltage and its intended reference.



(b) Actual PV voltages (v_{pv1}) and (v_{pv2}).

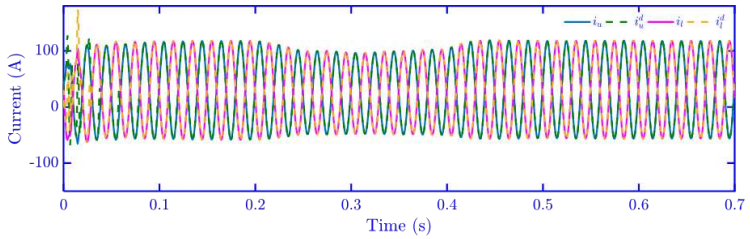


(c) Active power injected into the grid from PV panels.

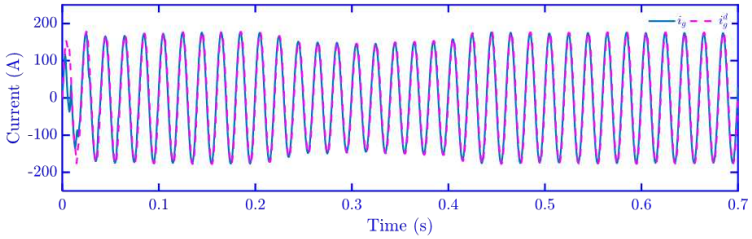
Fig. 12: Dynamic performance of the proposed control strategy under temperature variation: (a) DC bus voltage, (b) PV voltages, and (c) Grid-injected power.

6 Conclusion

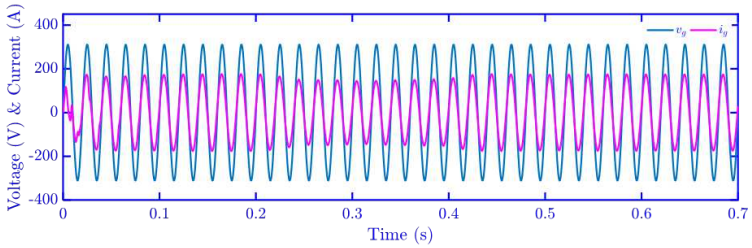
This paper has investigated the control of a single-phase grid-connected photovoltaic system based on a modular multilevel converter (PV–MMC), with particular emphasis on addressing its inherent nonlinear dynamics and multi-objective control requirements. A nonlinear control strategy based on the backstepping approach, supported by Lyapunov stability analysis, has been developed to ensure stable and reliable system operation. The proposed control framework achieves several key objectives simultaneously, including precise tracking of arm current references, effective balancing of PV voltages, unity power factor operation at the grid interface, and optimal power extraction from the photovoltaic source. The inner current loop ensures accurate current regulation and contributes to power factor correction, while the outer voltage loop enables efficient maximum power point tracking and maintains voltage balance across the system. The stability of the closed-loop system has been analytically validated



(a) Currents of the upper and lower arm.



(b) Actual grid current and its reference.

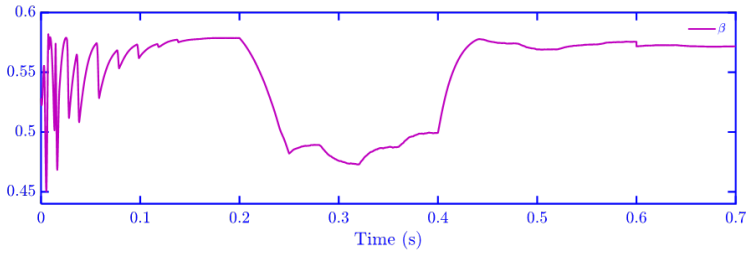


(c) Grid voltage and current showing PFC performance.

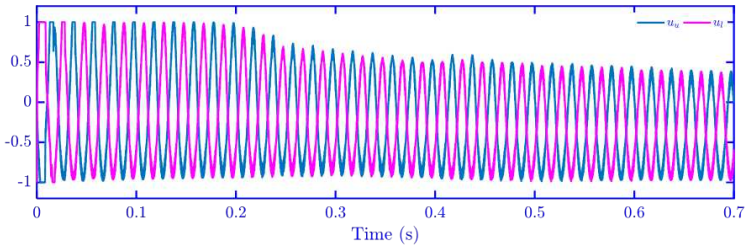
Fig. 13: Dynamic performance of the proposed control strategy under temperature variation: (a) Arm currents, (b) Grid current, (c) PFC performance.

using Lyapunov theory, guaranteeing the asymptotic convergence of tracking errors. In addition, simulation results under both nominal and varying operating conditions confirm the effectiveness of the proposed approach, highlighting its robustness, fast dynamic response, and good steady-state performance.

Overall, the proposed nonlinear control scheme offers a reliable and efficient solution for coordinated power management between the PV source and the grid. These results suggest that the proposed approach is well-suited for high-performance PV–MMC applications. Future work will focus on experimental validation and real-time implementation to further assess its practical feasibility.



(a) External signal β.



(b) Internal signals u_u and u_l.

Fig. 14: Dynamic performance of the proposed control strategy under temperature variation: (a) external control signal β, and (b) Internal signals.

Table 5: THD of the grid current under different temperature levels.

Temperature (°C)	**THD (%)**
15	0.22
25	0.14
45	0.27

References

[1] Swetha, S., Sumangala, B.: Solar photovoltaic power conversion using modular multilevel inverter. In: 2015 International Conference on Emerging Research in Electronics, Computer Science and Technology, pp. 387–391 (2015). https://doi.org/10.1109/SCES.2012.6199035 . IEEE

[2] Sinsel, S.R., Riemke, R.L., Hoffmann, V.H.: Challenges and solution technologies for the integration of variable renewable energy sources—a review. Renewable Energy **145**, 2271–2285 (2020) https://doi.org/10.1016/j.renene.2019.06.147

[3] Abouloifa, A., Aouadi, C., Lachkar, I., Boussairi, Y., Aourir, M., Hamdoun, A.:

Output-feedback nonlinear adaptive control strategy of the single-phase grid-connected photovoltaic system. Journal of Solar Energy **2018**(1), 6791056 (2018) https://doi.org/10.1155/2018/6791056

[4] Delavari, A., Kamwa, I., Zabihinejad, A.: A comparative study of different multilevel converter topologies for battery energy storage application. In: 2017 IEEE 30th Canadian Conference on Electrical and Computer Engineering, pp. 1–5 (2017). https://doi.org/10.1109/CCECE.2017.7946773 . IEEE

[5] Radomsky, L., Mallwitz, R.: Review, comprehensive analysis and derivation of analytical power loss calculation equations for two-to three-level midpoint clamped inverter topologies with hybrid switch configurations. Energies **16**(18), 6710 (2023) https://doi.org/10.3390/en16186710

[6] Katir, H., Abouloifa, A., Noussi, K., Lachkar, I., El Aroudi, A., Aourir, M., El Otmani, F., Giri, F.: Fault tolerant backstepping control for double-stage grid-connected photovoltaic systems using cascaded H-Bridge multilevel inverters. IEEE Control systems letters **6**, 1406–1411 (2021) https://doi.org/10.1109/LCSYS.2021.309510

[7] Nabae, A., Takahashi, I., Akagi, H.: A new neutral-point-clamped PWM inverter. IEEE Transactions on industry applications **IA-17**(5), 518–523 (1981) https://doi.org/10.1109/tia.1981.4503992

[8] Fahim, R.A., Biswas, S.P., Hosain, M.K., Hossain, S., Mondal, S., Islam, M.R., Fekih, A.: Improved switching technique to mitigate THD and power loss of NPC inverters. IEEE Transactions on Applied Superconductivity **34**(8), 1–5 (2024) https://doi.org/10.1109/TASC.2024.3420303

[9] Meynard, T.A., Foch, H., Thomas, P., Courault, J., Jakob, R., Nahrstaedt, M.: Multicell converters: basic concepts and industry applications. IEEE transactions on industrial electronics **49**(5), 955–964 (2002) https://doi.org/10.1109/TIE.2002.803174

[10] Maheswari, K.T., Bharanikumar, R., Arjun, V., Amrish, R., Bhuvanesh, M.: A comprehensive review on cascaded H-Bridge multilevel inverter for medium voltage high power applications. Materials Today: Proceedings **45**, 2666–2670 (2021) https://doi.org/10.1016/j.matpr.2020.11.519

[11] Taha, T.A., Shalaby, M., Wahab, N.I.A., Zaynal, H.I., Hassan, M.K., Al-Sowayan, S., Alawad, M.A.: Recent advancements in multilevel inverters: topologies, modulation techniques, and emerging applications. Symmetry **17**(7), 1010 (2025) https://doi.org/10.3390/sym17071010

[12] Sharma, B., Manna, S., Saxena, V., Raghuvanshi, P.K., Alsharif, M.H., Kim, M.-K.: A comprehensive review of multi-level inverters, modulation, and control for grid-interfaced solar PV systems. Scientific reports **15**(1), 661 (2025) https:

//doi.org/10.1038/s41598-024-84296-1

[13] Alotaibi, S., Darwish, A.: Modular multilevel converters for large-scale grid-connected photovoltaic systems: A review. Energies **14**(19), 6213 (2021) https://doi.org/10.3390/en14196213

[14] El Boudali, A., Abouloifa, A., Lachkar, I., Aourir, M., Aouadi, C., Arich, O., Hourri, N.: Modeling and control of single-phase modular multilevel converter using backstepping approach. In: International Symposium on Automatic Control and Emerging Technologies, pp. 808–816 (2023). https://doi.org/10.1007/978-981-97-0126-171 . Springer

[15] Marquardt, R.: Current rectification circuit for voltage source inverters with separate energy stores replaces phase blocks with energy storing capacitors. German Patent (DE10103031A1) **25** (2002)

[16] Samimi, S., Gruson, F., Delarue, P., Colas, F., Belhaouane, M.M., Guillaud, X.: MMC stored energy participation to the DC bus voltage control in an HVDC link. IEEE Transactions on power delivery **31**(4), 1710–1718 (2016) https://doi.org/10.1109/TPWRD.2016.2540926

[17] Gnanarathna, U., Chaudhary, S.K., Gole, A., Teodorescu, R.: Modular multilevel converter based HVDC system for grid connection of offshore wind power plant. In: 9th IET International Conference on AC and DC Power Transmission (ACDC 2010), pp. 1–5 (2010). https://doi.org/10.1049/cp.2010.0984 . IET

[18] Parker, M.A., Ran, L., Finney, S.J.: Distributed control of a fault-tolerant modular multilevel inverter for direct-drive wind turbine grid interfacing. IEEE Transactions on Industrial Electronics **60**(2), 509–522 (2012) https://doi.org/10.1109/TIE.2012.2186774

[19] Antonopoulos, A., Ängquist, L., Norrga, S., Ilves, K., Harnefors, L., Nee, H.-P.: Modular multilevel converter AC motor drives with constant torque from zero to nominal speed. IEEE Transactions on Industry Applications **50**(3), 1982–1993 (2013) https://doi.org/10.1109/ECCE.2012.6342746

[20] Zhang, Y., Ravishankar, J., Fletcher, J., Li, R., Han, M.: Review of modular multilevel converter based multi-terminal HVDC systems for offshore wind power transmission. Renewable and Sustainable Energy Reviews **61**, 572–586 (2016) https://doi.org/10.1016/j.rser.2016.01

[21] Allebrod, S., Hamerski, R., Marquardt, R.: New transformerless, scalable modular multilevel converters for HVDC-transmission. In: 2008 IEEE Power Electronics Specialists Conference, pp. 174–179 (2008). https://doi.org/10.1109/PESC.2008.4591920 . IEEE

[22] Lesnicar, A., Marquardt, R.: An innovative modular multilevel converter topology

suitable for a wide power range. In: 2003 IEEE Bologna Power Tech Conference Proceedings,, vol. 3, p. 6 (2003). https://doi.org/10.1109/PTC.2003.1304403 . IEEE

[23] Glinka, M., Marquardt, R.: A new AC/AC multilevel converter family. IEEE Transactions on Industrial Electronics **52**(3), 662–669 (2005) https://doi.org/10.1109/TIE.2005.843973

[24] Debnath, S., Qin, J., Bahrani, B., Saeedifard, M., Barbosa, P.: Operation, control, and applications of the modular multilevel converter: A review. IEEE Transactions on Power Electronics **30**(1), 37–53 (2015) https://doi.org/10.1109/TPEL.2014.2309937

[25] Saeedifard, M., Iravani, R.: Dynamic performance of a modular multilevel back-to-back HVDC system. IEEE Transactions on Power Delivery **25**(4), 2903–2912 (2010) https://doi.org/10.1109/TPWRD.2010.2050787

[26] Zhao, J., Jia, Y., Zhang, G., An, H., Zhao, T.: Sub-synchronous oscillation robust damping method for HVDC with embedded energy storage. Electronics **14**(13), 2599 (2025) https://doi.org/10.3390/electronics14132599

[27] Raj, R., Elmouatamid, A., Swain, A., Pong, P.W.: Critical review of hybrid modular multilevel converters for HVDC transmission in offshore wind energy. Energy Reports **14**, 1761–1778 (2025) https://doi.org/10.1016/j.egyr.2025.07.017

[28] Tian, Y., Konstantinou, G.: Reliability analysis of modular multilevel converters in MVDC applications. e-Prime-Advances in Electrical Engineering, Electronics and Energy **9**, 100671 (2024) https://doi.org/10.1016/j.prime.2024.100671

[29] Hagiwara, M., Akagi, H.: Control and experiment of pulsewidth-modulated modular multilevel converters. IEEE transactions on power electronics **24**(7), 1737–1746 (2009) https://doi.org/10.1109/TPEL.2009.2014236

[30] Ishfaq, M., Uddin, W., Zeb, K., Khan, I., Islam, S.U., Khan, M.A., Kim, H.J.: Output current control of modular multilevel converter using backstepping controller. In: 2019 15th International Conference on Emerging Technologies (ICET), pp. 1–5 (2019). https://doi.org/10.1109/ICET48972.2019.8994598 . IEEE

[31] Kadhum, H., Watson, A.J., Rivera, M., Zanchetta, P., Wheeler, P.: Model predictive control of a modular multilevel converter with reduced computational burden. Energies **17**(11), 2519 (2024) https://doi.org/10.3390/en17112519

[32] Alia, I., Merzouk, I., Rezaoui, M.M., Rezk, H., Lashab, A.: Output current observation and control of grid-connected modular multilevel converter using a simplified super twisting algorithm sliding mode. Results in Engineering **25**, 104280 (2025) https://doi.org/10.1016/j.rineng.2025.104280

[33] Arich, O., Abouloifa, A., El Boudali, A., Hourri, N.: Multi-objective cascaded controller design for multi-output DC-DC converter in grid-connected PV system. EPJ Web Conf. **380**, 02009 (2026) https://doi.org/10.1051/epjconf/202638002009

[34] Arich, O., Abouloifa, A., El Boudali, A., Al Numay, M.S., El Aroudi, A.: A multi-loop nonlinear control approach for a reduced-switch-count grid-tied PV system. Electric Power Systems Research **260**, 113352 (2026) https://doi.org/10.1016/j.epsr.2026.113352

[35] El Boudali, A., Abouloifa, A., Arich, O., Hourri, N.: ADRC strategy-based control for grid-connected pv system using a single-phase modular multilevel converter. EPJ Web Conf. **380**, 02010 (2026) https://doi.org/10.1051/epjconf/202638002010

[36] Barresi, M., Del Giudice, D., De Simone, D.: Three-phase reduced-sensor modular multilevel converter with distributed MPPT for PV integration based on extended kalman filter. Journal of Modern Power Systems and Clean Energy **14**(1), 368–382 (2025) https://doi.org/10.35833/MPCE.2024.001154

[37] Pablo, S., Bakir, Y.N., Martinez-Rodrigo, F., Herrero-de-Lucas, L.C., Rey-Boue, A.B.: Straightforward multilevel space vector modulation for a modular multilevel converter for PV generation. electronics **15**(1), 53 (2026) https://doi.org/10.3390/electronics15010053

[38] Chen, Y., Huang, M., Pan, S., El Aroudi, A., Zha, X.: Transient voltage and current stresses estimation of MMC-MTD system via discrete-time analysis. IEEE Transactions on Power Delivery **35**(6), 2821–2830 (2020) https://doi.org/10.1109/TPWRD.2020.2968389

[39] Salvadores, T., Pereda, J., Rojas, F.: Power imbalance analysis of modular multilevel converter with distributed energy systems. IEEE Open Journal of the Industrial Electronics Society **5**, 109–121 (2024) https://doi.org/10.1109/OJIES.2024.3361167

[40] Ishfaq, M., Uddin, W., Zeb, K., Khan, I., Ul Islam, S., Adil Khan, M., Kim, H.J.: A new adaptive approach to control circulating and output current of modular multilevel converter. Energies **12**(6), 1118 (2019) https://doi.org/10.3390/en12061118

[41] Uddin, W., Zeb, K., Adil Khan, M., Ishfaq, M., Khan, I., Islam, S.u., Kim, H.-J., Park, G.S., Lee, C.: Control of output and circulating current of modular multilevel converter using a sliding mode approach. Energies **12**(21), 4084 (2019) https://doi.org/10.3390/en12214084

[42] Bärnklau, H., Gensior, A., Rudolph, J.: A model-based control scheme for modular multilevel converters. IEEE Transactions on Industrial Electronics **60**(12),

5359–5375 (2012) https://doi.org/10.1109/TIE.2012.2236997

[43] Riar, B.S., Geyer, T., Madawala, U.K.: Model predictive direct current control of modular multilevel converters: Modeling, analysis, and experimental evaluation. IEEE Transactions on Power Electronics **30**(1), 431–439 (2014) https://doi.org/10.1109/TPEL.2014.2301438

[44] Yang, S., Tang, Y., Wang, P.: Open-circuit fault diagnosis of switching devices in a modular multilevel converter with distributed control. In: 2017 IEEE Energy Conversion Congress and Exposition, pp. 4208–4214 (2017). https://doi.org/10.1109/ECCE.2017.8096729 . IEEE

[45] Xiao, Q., Mu, Y., Jia, H., Jin, Y., Hou, K., Yu, X., Teodorescu, R., Guerrero, J.M.: Modular multilevel converter based multi-terminal hybrid AC/DC microgrid with improved energy control method. Applied Energy **282**, 116154 (2021) https://doi.org/10.1016/j.apenergy.2020.116154

[46] Abo-Khalil, A.G., Bashir, S.B., Farag, M.M., Ismail, A.A.A., Hamid, A.-K., Mbungu, N.T., Bansal, R.C., Elnady, A., Patel, N.: Direct modulation in MMC-based multiterminal hybrid microgrid: A solution for arm capacitor voltage balancing under unbalanced power distribution. International Journal of Electrical Power & Energy Systems **162**, 110274 (2024) https://doi.org/10.1016/j.ijepes.2024.110274

[47] Arich, O., Abouloifa, A., Lachkar, I., Echalih, S., Aourir, M., El Boudali, A., Hourri, N.: Nonlinear controller design for photovoltaic powered single-inductor dual-output boost DC-DC converter. In: International Symposium on Automatic Control and Emerging Technologies, pp. 475–484 (2023). https://doi.org/10.1007/978-981-97-0126-142 . Springer

[48] Hourri, N., Abouloifa, A., Hekss, Z., Lachkar, I., Arich, O., El Boudali, A.: Nonlinear control of three phase single stage grid connected PV system through half bridge power inverter. In: International Symposium on Automatic Control and Emerging Technologies, pp. 282–292 (2023). https://doi.org/10.1007/978-981-97-0126-125 . Springer

[49] Perez, M.A., Bernet, S., Rodriguez, J., Kouro, S., Lizana, R.: Circuit topologies, modeling, control schemes, and applications of modular multilevel converters. IEEE transactions on power electronics **30**(1), 4–17 (2014) https://doi.org/10.1109/TPEL.2014.2310127

[50] Kinhekar, N., Ghat, M., *et al.*: Grid connection of modular multilevel converter. In: 2016 IEEE 1st International Conference on Power Electronics, Intelligent Control and Energy Systems, pp. 1–6 (2016). https://doi.org/10.1109/ICPEICES.2016.7853562 . IEEE

[51] Solas, E., Abad, G., Barrena, J., Carcar, A., Aurtenetxea, S.: Modulation of

modular multilevel converter for HVDC application. In: Proceedings of 14th International Power Electronics and Motion Control Conference EPE-PEMC 2010, pp. 2–84 (2010). https://doi.org/10.1109/EPEPEMC.2010.5606876 . IEEE